Article

Effect of Geochemical Reactivity on ScCO$_2$–Brine–Rock Capillary Displacement: Implications for Carbon Geostorage

Felipe Cruz *, Son Dang (ID)**, Mark Curtis and Chandra Rai**

Mewbourne School of Petroleum and Geological Engineering, University of Oklahoma,
Norman, OK 73019-1003, USA; dangthaison@ou.edu (S.D.); mcurtis@ou.edu (M.C.); crai@ou.edu (C.R.)
* Correspondence: felipecruz@ou.edu

Abstract: The displacement efficiency of supercritical CO$_2$ (scCO$_2$) injection in the storage zone and its primary trapping mechanism in the confining zone are strongly tied to the capillary phenomenon. Previous studies have indicated that the capillary phenomenon can be affected by geochemical reactivity induced by scCO$_2$ dissolution in formation brine. To quantify such changes, thin disk samples representing a sandstone storage reservoir, siltstone confining zone, and mudstone confining zone were treated under a scCO$_2$-enriched brine static condition for 21 days at 65 °C and 20.7 MPa. Geochemical alterations were assessed at the surface level using scanning electron microscopy coupled with energy-dispersive X-ray spectroscopy and X-ray fluorescence. Before and after treatment, the wettability of the scCO$_2$–brine–rock systems was determined using the captive-bubble method at fluid-equilibrated conditions. Pore size distributions of the bulk rocks were obtained with mercury injection capillary pressure, nuclear magnetic resonance, and isothermal nitrogen adsorption. The results indicate the dissolution of calcite at the surface, while other potentially reactive minerals (e.g., clays, feldspars, and dolomite) remain preserved. Despite alteration of the surface mineralogy, the measured contact angles in the scCO$_2$–brine–rocks systems do not change significantly. Contact angle values of $42 \pm 2°$ for sandstone and $36 \pm 2°$ for clay-rich siltstone/calcite-rich mudstone were determined before and after treatment. The rocks studied here maintained their water-wettability at elevated conditions and after geochemical reactivity. It is also observed that surface alteration by geochemical effects did not impact the pore size distributions or porosities of the thin disk samples after treatment. These results provide insights into understanding the impact of short-term geochemical reactions on the scCO$_2$–brine capillary displacement in the storage zone and the risks associated with scCO$_2$ breakthrough in confining zones.

Keywords: carbon geostorage; geochemical reactivity; supercritical CO$_2$; wettability; capillary pressure

1. Introduction

Carbon geostorage (CGS) is considered a primary solution to limit the global average temperature according to Paris Agreement and achieve net-zero emissions [1]. In CGS, gaseous CO$_2$ is captured at large-scale point sources and injected in porous geological formations at depths beyond 800 m to ensure a supercritical state (scCO$_2$), hence maximizing storage resources [2]. Sandstones are frequently chosen as host rocks for CGS because of their high injectivity and storage capacity [3,4], whereas siltstones [5–8] and mudstones [9,10], characterized by low permeability, are well-suited as confining zones. In addition to the macroscopic fluid displacement within the host rock, which is a function of its heterogeneity, the efficiency of the storage process is intricately linked to microscopic displacement factors such as interfacial tension (IFT), wettability, and pore size distribution [11–13]. During and after brine displacement, scCO$_2$ is primarily trapped by capillary forces acting on the confining zone (structural trapping) and in the storage zone (residual trapping) [14]. Secondary immobilization of scCO$_2$ occurs by long-term geochemical interactions with formation fluids and rock, including dissolution in fluid (solubility trapping)

and formation of stable mineral species (mineral trapping) [15]. Understanding the outcomes of these chemical reactions to the $scCO_2$ microscopic displacement and trapping mechanisms is a challenge, which requires exposure experiments to be conducted at different conditions representing time-spatial distribution within the storage and confining zones [16,17].

The influencing factors on the $scCO_2$ microscopic displacement and its primary trapping mechanisms can be simplified by the capillary phenomenon [17,18]. The net pressure required to displace a non-wetting phase (e.g., $scCO_2$) through a pore throat saturated by a wetting phase (e.g., brine) is given by the Laplace equation [19,20] (Equation (1)):

$$P_c = P_{scCO_2} - P_{H_2O} = \frac{2\gamma\cos\theta}{r}, \tag{1}$$

where P_c is the capillary pressure, γ is the $scCO_2$–brine interfacial tension, θ is the contact angle, and r is the pore throat radius. As described in Equation (1), the capillary pressure is directly proportional to the product of the tension formed between the fluid phases and the cosine of the contact angle, and inversely proportional to the pore size. If the $scCO_2$ pressure exceeds the breakthrough pressure in the confining zone, upward fluid migration takes place, and the maximum $scCO_2$ height that can be stored in the caprock (h) is given by Equation (2):

$$h = \frac{2\gamma\cos\theta}{\Delta\rho g r}, \tag{2}$$

where $\Delta\rho$ is the difference in fluid densities between $scCO_2$ and brine, g is the gravity constant, and r is the connected pore throat radius during breakthrough [21]. Equation (2) shows that in addition to the capillary properties, knowledge of fluid densities in $scCO_2$–brine systems is essential to determine the capillary seal capability [22].

Regarding the interfacial tension, several authors have shown that the IFT of CO_2–H_2O systems is primarily controlled by the density difference of the two fluid phases [23–26]. It is generally agreed that the IFT follows a bilinear trend with $\Delta\rho$. For gaseous CO_2, the IFT decreases steeply and linearly with decreasing $\Delta\rho$ (alternatively, increasing pressure) due to an increase in gas solubility [21]. Above the $scCO_2$ condition ($\Delta\rho$~600 kg/m^3, ~7.3 MPa, ~31 °C), the IFT decreases mildly, reaching a pseudo plateau at ~26 $\pm$ 2 mN/m [23,27]. The pseudo-plateau IFT is independent of temperature [23], increases linearly with salt molality [23,28,29], and is more pronounced in the presence of bivalent cations [23,28,29].

Numerous authors have described the wettability of $scCO_2$–brine–rock systems [30–74]. During CGS, water-wettability over $scCO_2$ is often preferred because it limits upward vertical migration and increases residual trapping in the reservoir [75–77], as well as increasing structural trapping, thus reducing the risk of $scCO_2$ breakthrough in the confining zone [78,79]. Figure 1 shows a literature compilation of $scCO_2$–brine–rock contact angles as a function of pressure for sandstone [66], limestone [66], dolomite [55], fine-grained caprocks [49], and source rock [58], measured at similar temperatures (~50 °C). A water-wet behavior with respect to $scCO_2$ is observed for most rocks. An exception is dolomite, which has lower hydrophilicity and shows strong negative pressure dependence with cos θ [55]. Aside from pressure, other parameters such as temperature and salinity exhibit less clear influence on θ. Studies conducted on quartz show increasing θ with increasing temperatures [40,44,51,66]; sandstones exhibit no clear trend [62,66]; whereas calcite [56] and carbonate [32] show decreasing θ trends with increasing temperature. Regarding salinity, some papers report quartz and calcite surfaces becoming slightly less water-wet in high salinity [38,56,66]. However, studies conducted on real rocks show either no trend in θ with salinity for a silica/dolomite-rich shale caprock [54], or a slight decrease with salinity for sandstone [62]. Inconsistencies in θ values are mostly attributed to differences in surface cleaning methods [44,71], rock heterogeneity [31], and surface roughness [57,62].
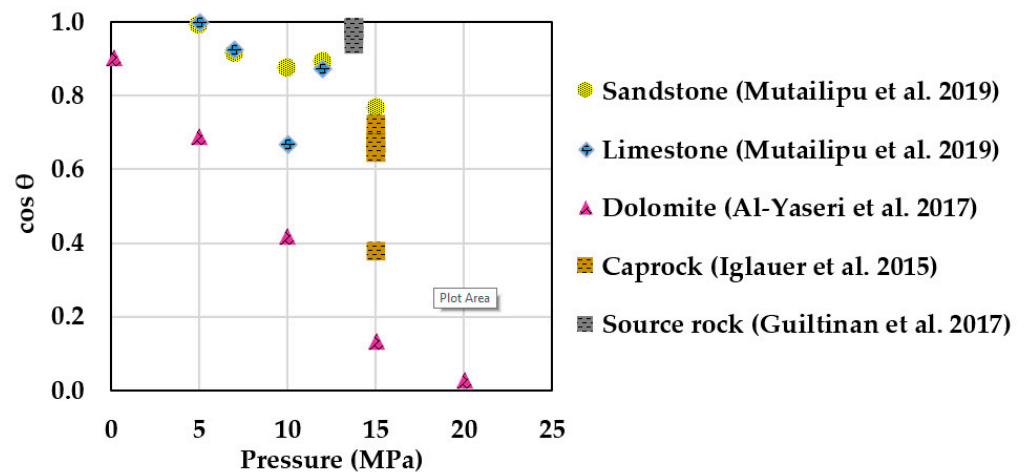
Figure 1. ScCO$_2$–brine–rock wettability as function of pressure at similar temperature (~50 °C) and salinity conditions. Most rocks exhibit water-wettability with respect to scCO$_2$ even at elevated pressures. An exception is dolomite, showing strong negative pressure dependence on θ (lower hydrophilicity). Note: sandstone [66], limestone [66], and source rock [58] contact angle values were conducted in static measurements. Caprock [49] represents receding contact angles, while dolomite [55] is an average of retreating and advancing values.
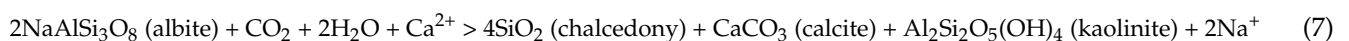
The interaction between scCO$_2$ and brine in the subsurface can trigger geochemical reactions with the rock and potentially impact the microscopic displacement and trapping mechanisms during CGS. These geochemical reactions are generally classified as short- and long-term reactions [80,81]. At the early stage, the dissolution of CO$_2$ in brine occurs, generating carbonic acid, which further ionizes into carbonate and bicarbonate ions, ultimately reducing the pH down to ~3 [80,82,83]:

$$CO_2 \ (gas) + H_2O \rightleftharpoons H_2CO_3 \tag{3}$$

$$H_2CO_3 \rightleftharpoons H^+ + HCO_3^- \tag{4}$$

$$HCO_3^- \rightleftharpoons H^+ + CO_3^- \tag{5}$$

The increase in H$^+$ species in the brine accelerates carbonate dissolution given their fast reactivity in acidic environments [84]. Among carbonates, calcite exhibits the largest dissolution rate, being ~2–3 and ~3–4 orders of magnitude faster than dolomite and siderite, respectively [85–87]. During calcite dissolution, the reactant is consumed quickly, and the reaction ceases at an equilibrium pH of 4.5–5.0 [80,83]:

$$CaCO_3 \ (calcite) + H^+ \rightleftharpoons Ca^{2+} + HCO_3^- \tag{6}$$

Alternatively, aluminosilicates such as feldspars, micas, and clays can yield more cations in the brine and buffer the pH up to ~8.0. However, their reaction rates are small and can take up to thousands of years to occur [80,83]. A secondary alteration of feldspars can occur when the concentration of calcium ions deriving from the dissolution of carbonates plus originally occurring in the brine is considerable [80,88]. An example is the dissolution of albite consuming Ca^{2+} and leading to the precipitation of calcite and kaolinite [80]:

$$2NaAlSi_3O_8 \ (albite) + CO_2 + 2H_2O + Ca^{2+} > 4SiO_2 \ (chalcedony) + CaCO_3 \ (calcite) + Al_2Si_2O_5(OH)_4 \ (kaolinite) + 2Na^+ \tag{7}$$

Recent studies have evaluated the role of geochemical alterations induced by scCO$_2$–brine interactions in the capillary properties of the storage zone [89–91] and confining zone [60,69,73,92–98]. Due to their high reactivity, limestones are generally the storage rock of focus, given that the reactivity

of sandstones (mainly quartz) is extremely slow and pH-independent [16,83]. Dynamic $scCO_2$-enriched brine injection tests on limestone cores show strong calcite dissolution and enlargement of pore throats in the inlet of the core, followed by slight mineral precipitation in the far region [89,90]. Additionally, an increase in the limestone $scCO_2$-wettability was observed after $scCO_2$-enriched brine treatment [90,91].

With respect to confining zones, most $scCO_2$ treatment studies were conducted on crushed samples, observing significant geochemical alteration in the form of dissolution and/or precipitation of preferentially carbonate minerals [92,94,95,98,99]. Mouzakis, et al. [92] reported an increase in porosity and connectivity in all pore length scales of a carbonate-rich shale. Sanguinito, et al. [94], Goodman, et al. [95] performed experiments on the same Utica Shale (clay/calcite-rich) but varying reactor fluid, from dry $scCO_2$ to $scCO_2$-enriched deionized water (DIW), respectively. They reported increased reactivity when water was introduced into the system. Some studies indicate that dry $scCO_2$ can also affect the hydration of clays by possibly releasing interstitial water [60,94]. Regarding wettability alteration, Qin, et al. [60] described an increase in water contact angles ($57 \pm 2°$ to $69 \pm 2°$) on quartz/clay-rich shales after exposure to dry $scCO_2$ for 12 days. However, their θ measurements were conducted at ambient conditions and do not reflect the equilibrium between $scCO_2$–brine in the subsurface [76]. Conversely, Gholami, et al. [69] conducted equilibrated $scCO_2$–DIW θ measurements on quartz/clay-rich shales exposed to $scCO_2$ for 6 months. They reported an average increase from $40 \pm 5°$ to $49 \pm 5°$, along with surface dissolution of quartz and precipitation of kaolinite. To the best of our knowledge, changes in $scCO_2$–brine–rock wettability by geochemical reactivity of carbonates present in confining zones and the extent of reactivity in the pore size distributions of intact rock samples have not been addressed.

The principal aim of this study is to evaluate the impact of geochemical reactivity on the $scCO_2$–brine–rock wettability and pore size distribution (PSD) of quartz, clay, and carbonate-rich intact rocks, both before and after treatment with $scCO_2$. The specific objectives are as follows: (i) assess geochemical alterations on thin disk samples after exposing to $scCO_2$-enriched brine environment at 20.7 MPa and 65 °C for 21 days, (ii) monitor changes in fluid-equilibrated $scCO_2$–brine–rock contact angles, with a particular emphasis on the impact of surface reactivity on the wettability of the $scCO_2$–brine–rock system under elevated pressure conditions (~20 MPa), and (iii) determine alterations in PSD using three different methods: mercury injection capillary pressure (MICP), nuclear magnetic resonance (NMR), and isothermal nitrogen (N_2) adsorption, and analyze the resulting data to assess the effects of geochemical reactions on the PSD of the thin disk samples. This study aims to provide insights into how geochemical reactions occurring within an experimental timeframe may influence the wettability and pore structure of rocks relevant to carbon geostorage (CGS).

2. Materials and Methods

2.1. Samples Description

For this study, we selected potential storage and confining zone rock samples varying in mineralogy and petrophysical properties (Table 1). The core samples were obtained from drilling sites where horizontal plugs (~2.5 cm diameter and length) were extracted in the "as-received" state. The plugs were cleaned using Soxhlet extraction with 80/20 toluene/methanol solution to remove hydrocarbons, water, and salt, and dried at 100 °C until weight stabilized. Total porosity was measured using the protocol described in our previous work [100]. Mineralogy determined using transmission Fourier transform infrared spectroscopy (FTIR) [101,102] and microstructural examination with scanning electron microscopy (SEM) indicates that sample S1 is a quartz-rich sandstone, S2 is a quartz/clay-rich siltstone, and S3 is a finer-grained carbonate/clay-rich mudstone. Total organic carbon (TOC) measured with the LECO® method on the mudstone (S3) shows low TOC (~2.0%). To prepare the sample for our measurements, four adjacent thin disks (~0.6 cm length) were cut from each plug. Vertical heterogeneity from the same plug was minimized by conducting several X-ray fluorescence (XRF) measurements on the surface of each disk and confirming low elemental variation. To minimize surface roughness, the measurement surface of each disk was subjected to fine polishing up to 2400 grit sandpaper followed by ion-milling (Fischione 1060 SEM, Export, USA). Then, MICP data were taken on one "untreated" disk from each sample (Table 1). The other disks were used in other pre-treatment measurements such as (1) surface characterization using SEM coupled with energy dispersive X-ray spectroscopy (EDS) (detailed imaging procedure can be found in Curtis, et al. [103]), (2) fluid-equilibrated $scCO_2$–brine–rock captive-bubble contact angle (θ) measurements, (3) NMR T_2 porosity measurements, and (4) isothermal N_2 adsorption. After initial measurements, the samples were exposed to static $scCO_2$-enriched brine. The same

measurements were conducted after exposure to assess changes in the samples due to scCO$_2$-enriched brine exposure.

Table 1. Mineralogy, porosity, TOC, and MICP measurements on the samples used in this study.

Sample	Lithology	Quartz + Feldspars (wt.%)	Clays (wt.%)	Carbonates (wt.%)	Porosity (%)	TOC (wt.%)	Mean Pore Radius (nm)
S1	Sandstone	80	14	6	9.3	-	440
S2	Siltstone	47	40	13	7.1	-	7.7
S3	Mudstone	14	31	55	5.9	2.0	3.0

Note: mean pore radius determined with MICP measurement.

2.2. scCO$_2$-Enriched Brine Treatment

According to Gaus, et al. [80], most caprock reactivity induced by scCO$_2$ will occur close to the boundary of the reservoir. For that reason, the samples used in this study were treated in a scCO$_2$-enriched brine condition in order to maintain maximum brine saturation and avoid undesirable effects such as drying out by CO$_2$ [104,105]. The brine was synthetically formulated using a 2.5 wt.% KCl solution (DIW). For the scCO$_2$-enriched brine treatments, each sample was exposed in individual reactors (Parr Instrument, Moline, IL, USA) that can operate in pressure and temperature conditions up to 58 MPa and 350 °C, respectively. The reactors were cleaned between each test with toluene, isopropanol, and acetone to avoid cross-contamination. To determine the experimental conditions, a desirable injection depth of 2000 m was selected [106]. Assuming a hydrostatic pressure gradient for brine of ~1.05 $\frac{MPa}{100m}$ and temperature gradient of ~24 $\frac{°C}{km}$, experimental conditions of ~20.7 MPa and ~65 °C were determined. The exposure time selected was 21 days, which, according to previous studies, is sufficient to observe geochemical reactions such as carbonate dissolution/precipitation [92,94,95,98,99] and clay reactivity [60,94]. Note that given the mineral reaction rates, quartz dissolution [69] and secondary feldspar alteration [80] are not expected to be observed since they could take up to 180 days and 19 months to experimentally occur, respectively. After selecting the exposure conditions, the samples were placed in the reactors inside an oven and immersed in brine at a ~10:1 brine/rock volume ratio. Then, scCO$_2$ was slowly introduced into the system using a piston pump (Teledyne ISCO, Lincoln, Dearborn, MI, USA) at a ~0.4 MPa/h pressure gradient to avoid microfracturing of samples. Pressure and temperature were monitored during the process. After exposure, the system was cooled and depressurized at the same gradient as injection and the samples were sequentially used in further measurements.

2.3. scCO$_2$–Brine–Rock Contact Angle Measurement

Several configurations have been used to measure the contact angle of scCO$_2$–brine–rock systems in subsurface conditions [64]. The captive-bubble technique was chosen (Figure 2) in order to keep the brine sample saturated during the measurement and avoid possible drying out if surrounded by a scCO$_2$ environment. The measurements were conducted using a drop shape analyzer (DSA100, Krüss GmbH, Hamburgh, Germany) coupled with an HPHT unit (Eurotechnica, Bargteheide, Germany) with a maximum working pressure and cell temperature of 69 MPa and 200 °C, respectively. Prior to the measurement, a brine-saturated sample was mounted on a custom-made, chemically inert holder (PEEK) that slides through a known outside diameter needle (~1.587 mm) that orients with the center of the sample. This orientation step allows the scCO$_2$ bubble to contact the ion-milled surface of the sample, reducing the roughness impact on θ and minimizing lateral heterogeneity. Then, roughly 30 mL of brine was introduced into the system until it covered the top surface of the sample. The unit was heated slowly up to 65 °C. ScCO$_2$ was injected from the top (gas cap), allowing diffusion into the brine and maintaining a constant pressure of 20.7 MPa, which was also monitored. After the fluid equilibration had taken place (~2 h), one scCO$_2$ bubble was carefully extruded from the needle using a separate dosing unit. Image calibration was performed, and the software (ADVANCE, version 1.10.0) recorded the static scCO$_2$–brine–rock contact angle over time. The exact same procedure was conducted on the samples after scCO$_2$–brine–rock treatment.
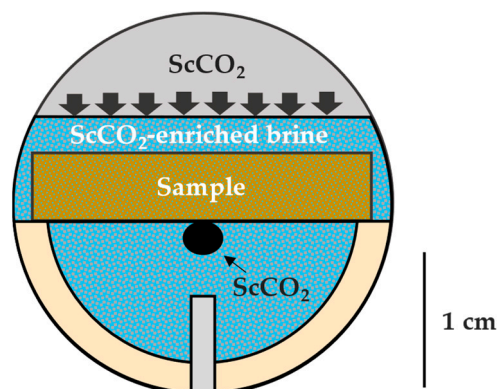
Figure 2. Schematic of the scCO$_2$–brine–rock captive-bubble measurement including approximate scale in centimeters. The brine surrounding the rock sample is enriched in scCO$_2$ diffusing downward from the "gas-cap" at desired pressure and temperature conditions. After equilibration, one scCO$_2$ bubble is carefully extruded from the needle (bottom), contacting the center of the ion-milled bottom surface of the sample.

2.4. Pore Size Distribution Measurements

Porosity and pore size distribution measurements were conducted before and after scCO$_2$ treatment. Pore throat size distributions (PTSDs) were obtained on clean and dried thin disk samples using MICP measurements (AutoPore IV, Micromeritics, Norcross, GA, USA). The AutoPore IV mercury porosimeter has a capability of 60,000 psi, which covers a nanopore throat radius of up to 1.5 nm [107]. For porosity, 12 MHz NMR T$_2$ measurements (GeoSpec II, Oxford Instruments, Abindgon, UK) were conducted on 2.5 wt.% KCl brine-saturated disk samples. In the NMR measurements, three disks were stacked in order to increase volume and enhance the signal-to-noise ratio (SNR). Echo spacing of 200 μs was selected for sample S1 (storage zone), while 100 μs was used in samples S2 and S3 (confining zone). Isothermal N$_2$ adsorption measurements (TriStar II, Micromeritics, Norcross, GA, USA) were conducted on the confining zones (S2 and S3) to assess changes in the nanopore structure. For the N$_2$ adsorption measurements, each sample was crushed, homogenized, and sieved into micrometer sizes (250–425 μm). N$_2$ adsorption pore size distributions were obtained with the density functional theory (DFT) using a slit-shaped model. Specific surface areas were determined with the Brunauer–Emmett–Teller (BET) method, fitting the adsorption data in the low relative pressure range (0.5–0.35).

3. Results

3.1. Geochemical Alteration

Figure 3 shows the backscattered electron (BSE) images of the three samples obtained over the same areas before and after scCO$_2$-enriched brine treatment. Figure 3a–c represent the microstructure before treatment of samples S1, S2, and S3, respectively. Images of the same areas for each sample after treatment are sequentially shown in Figure 3d–f. Before treatment, sample S1 is composed mainly of quartz grains and some clays (illite, chlorite, and kaolinite) filling the pore spaces. Sample S2 is covered by silicates, aluminosilicates, and minor carbonates. S3 is predominantly carbonate-rich, including clays, minor silicates, and pyrite (white). After treatment, no geochemical reactivity is observed on sample S1, except for salt precipitation. Conversely, sample S2 exhibits preferential dissolution of carbonate minerals (highlighted in red), while the main silicate and aluminosilicate framework remains preserved. Given the larger carbonate content of sample S3 (Table 1), it shows significant surface alteration by dissolution of carbonates after treatment. It is observed that other potentially reactive minerals such as clays and pyrite (white) are unaltered during this process.

Figure 4 shows BSE images on a strongly reacting area of the sample S3 before (Figure 4a) and after (Figure 4b) treatment. In Figure 4c, the spatial elemental mapping before treatment obtained with EDS shows predominantly calcite with minor amounts of silicate and dolomite. Figure 4d shows that, after treatment, calcite is the only carbonate mineral dissolved, whereas dolomite remains unaltered. XRF measurements performed before and after treatment at the surface of sample S3 indicate a reduction in the relative content of calcium oxide (CaO) from 55 wt.% to 14 wt.%, respectively.
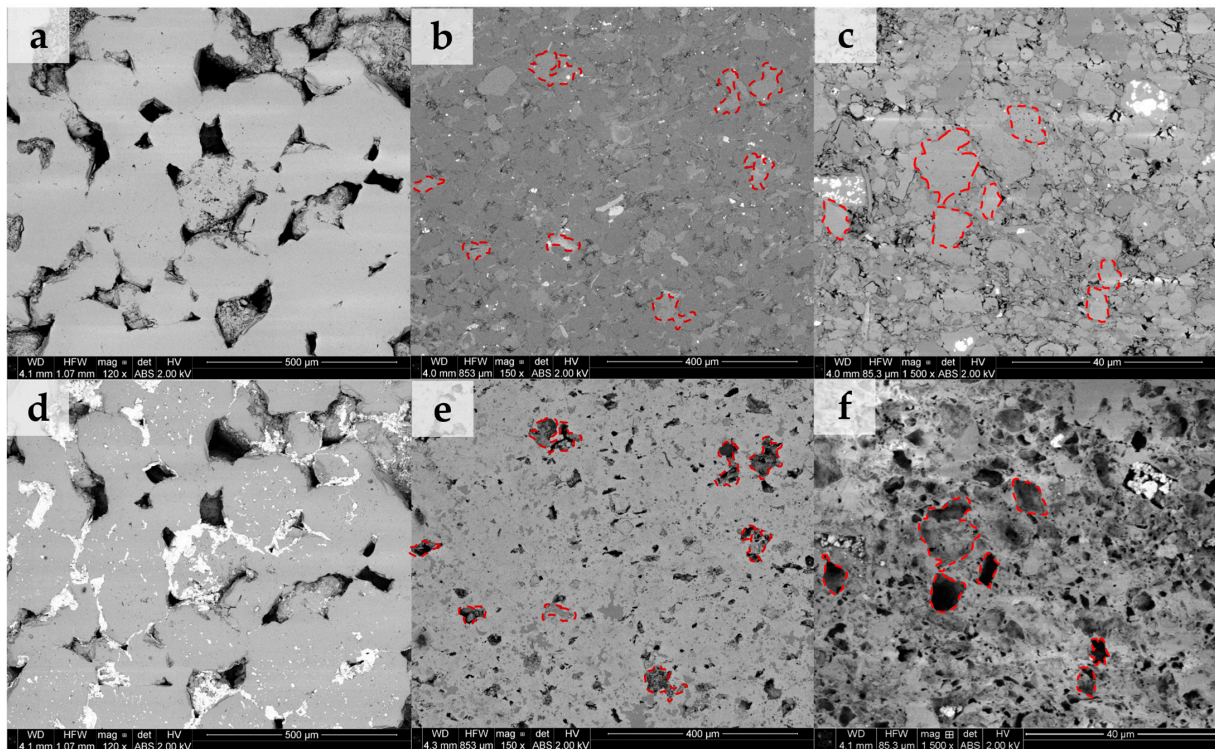
Figure 3. Backscattered images (BSEs) of the same sample area before and after scCO$_2$-enriched brine treatment. (**a**–**c**) represent areas before treatment for samples S1, S2, and S3, respectively. Their same areas after treatment are sequentially shown in (**d**–**f**). Sample S1 indicates no geochemical reactivity aside from salt precipitation. Sample S2 shows preferential dissolution of carbonates (highlighted in red), while the silicate/aluminosilicate framework remains preserved. Sample S3 reveals intense surface alteration by dissolution of carbonates, which was expected given their larger initial carbonate content. Other potentially reactive minerals such as clays and pyrite were little affected during the process.
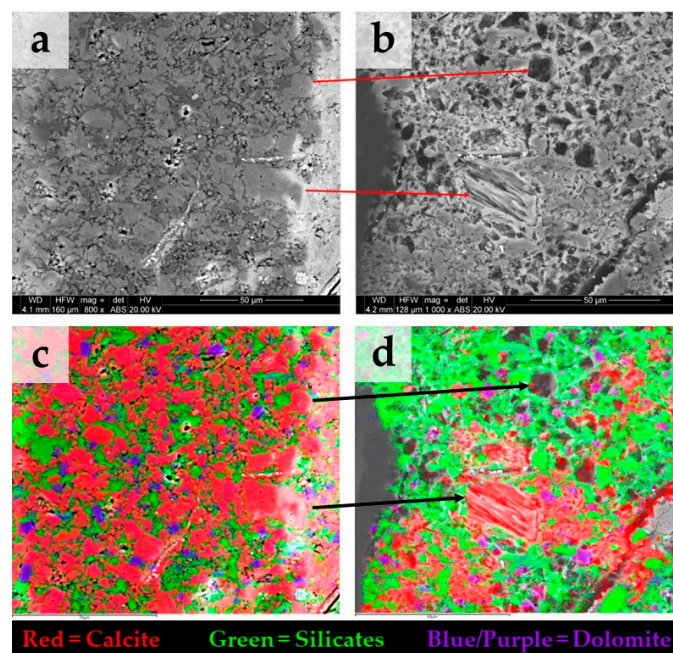

Figure 4. BSE images before (**a**) and after (**b**) treatment on the same area of sample S3 showing strong alteration due to carbonate dissolution. Note: in (**b**), the depicted image exhibits a slight displacement

relative to (**a**), while the arrows serve to locate the same calcite grains. (**c**) spatial elemental mapping with EDS before treatment, the area has predominantly calcite with minor amount of dolomite. (**d**) after treatment, calcite appears as the only mineral dissolved, while dolomite remains unaltered.

3.2. ScCO$_2$–Brine–Rock Wettability

Figure 5 shows the summary of the captive-scCO$_2$ bubble–brine–rock contact angle measurements conducted at the same experimental conditions (20.7 MPa, 65 °C) before and after scCO$_2$-enriched-brine treatment. Before treatment, contact angles of 42 ± 1°, 37 ± 1°, and 35 ± 2° are observed for samples S1, S2, and S3, respectively. These contact angle values are comparable to ones reported in the literature for sandstones, caprock, and source rocks at similar experimental conditions (Figure 1) [49,55,58,66]. It can be observed that these rocks maintain their water-wettability even at larger pressures up to ~20 MPa. After scCO$_2$-enriched brine treatment, negligible changes in contact angles are observed, despite the surface reactivity (primarily S3) shown in Figure 3. Trapping of surface bubbles can also be noted on sample S3, which develops during the fluid-equilibration phase and indicates that in-situ reactions could be taking place as the brine becomes saturated in scCO$_2$.
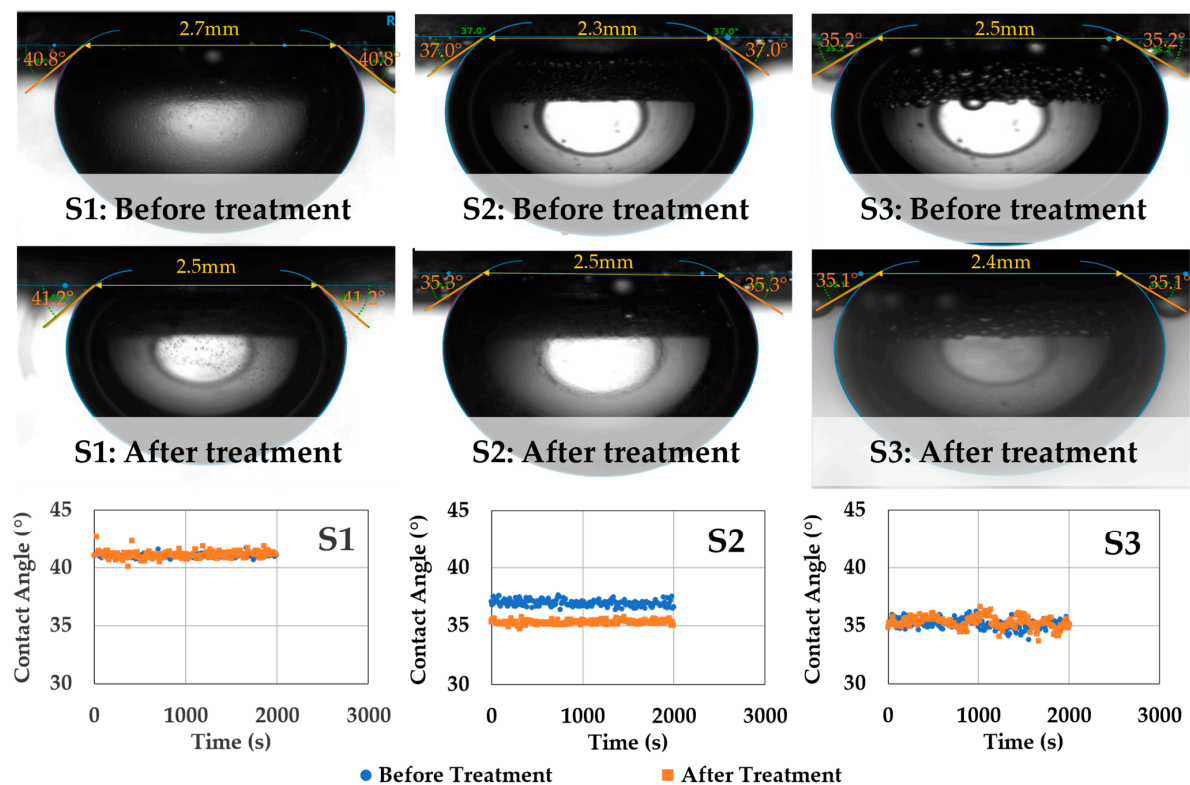

Figure 5. Summary of the scCO$_2$–brine–rock captive-bubble contact angle measurements before and after scCO$_2$ enriched brine treatment. The equilibrated contact angles remain unaltered despite surface alteration (primarily S3). The samples maintain their water-wettability even at elevated pressure (~20 MPa) and temperature (65 °C) conditions and after geochemical reactivity.

3.3. Pore Size Distribution

Pore size distribution alterations of the thin disk samples were assessed before and after scCO$_2$-enriched brine treatment with three different techniques. Figure 6 shows MICP incremental and cumulative pore throat size distributions (PTSDs) of the samples before and after treatment. Figure 6a–c represent the incremental curves for samples S1, S2, and S3, respectively. Their cumulative curves are sequentially shown in Figure 6d–f. The PTSD for sample S1 (storage zone) indicates initial intrusion in the 2–10 μm pore throat size range followed by a main peak between 200 and 600 nm. Conversely, the main peaks for the confining zone samples S2 and S3 are considerably lower, at around 6–10 nm and 2–4 nm, respectively. After treatment, little alteration is observed in the PTSD of samples S1 and

S2. Sample S3 indicates minor changes, aside from a slight increase in amplitude in the pore range of 100–1000 nm, followed by a drop in the main peak at 1–10 nm.
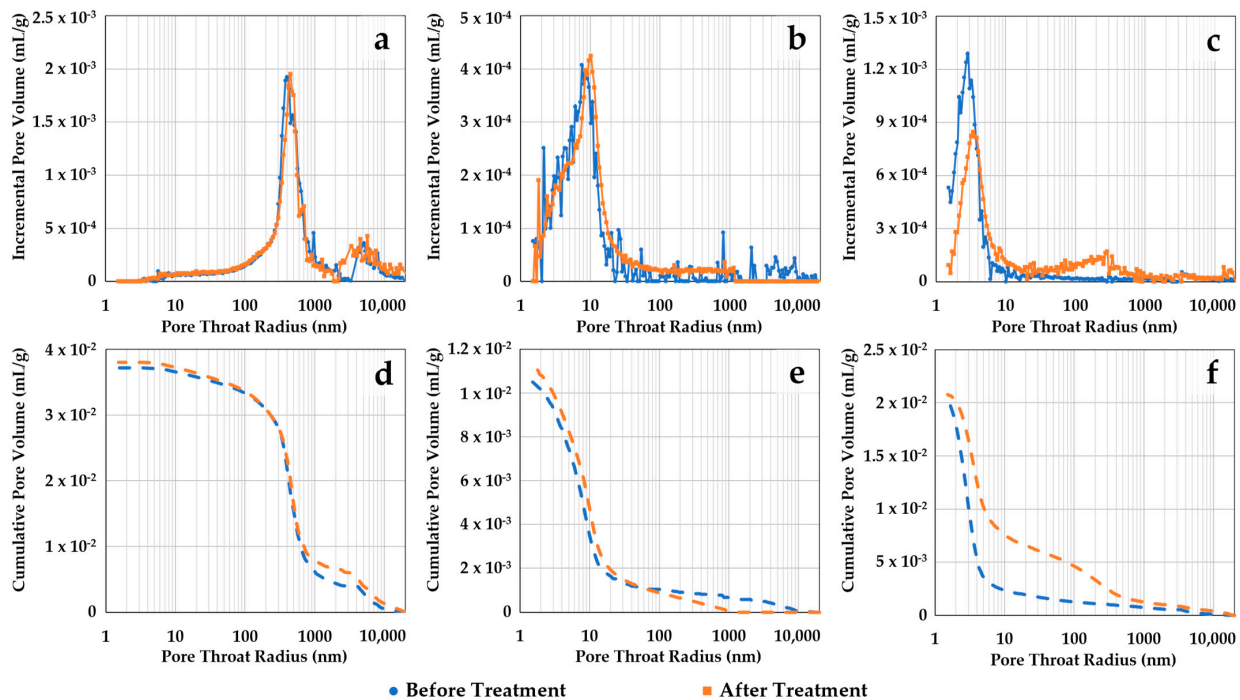

Figure 6. Pore throat size distributions (PTSDs) obtained with MICP before and after scCO$_2$-enriched brine treatment. The incremental curves for samples S1, S2, and S3 are shown in (**a**–**c**), respectively. Their cumulative curves are sequentially represented in (**d**–**f**). Little alteration is observed in the PTSD of the samples, aside from a small increase in amplitude in the 100–1000 nm range for sample S3 followed by a drop in the 1–10 nm range.

Figure 7 shows NMR T$_2$ porosity distributions of the three samples before and after scCO$_2$-enriched-brine treatment. Figure 7a–c represent the incremental curves for samples S1, S2, and S3, respectively. Their cumulative curves are sequentially shown in Figure 7d–f. Before treatment, sample S1 (storage zone) shows a main peak around 100 ms T$_2$ relaxation, while the main peaks for the confining samples S2 and S3 are in shorter T$_2$ times of ~1.1 ms and 0.8 ms, respectively. For the confining zone samples, the second small peak above 100 ms represents brine trapped in the surface irregularities of the samples. Nevertheless, the porosity distributions obtained with NMR indicate no significant alteration in the three samples after treatment. Sample S3 exhibits a small inflection in the spectrum after treatment around 1–20 ms, which does not impact the cumulative porosity within this range.

Figure 8 displays N$_2$ adsorption and desorption isotherms for confining zone samples S2 and S3 before (Figure 8a) and after (Figure 8b) scCO$_2$-enriched-brine treatment. These curves, along with hysteresis loop analysis, yield insights into pore structure and connectivity in tight porous media, such as shales [108–110]. Before treatment, both samples exhibited type IV isotherm characteristics with a distinctive hysteresis loop, indicating capillary condensation in meso/macro-pores [111]. There is no limiting uptake at high relative pressures (p/p^0), indicating an H3 hysteresis loop with slit-shaped pores forming plate-like structures [112]. A wider hysteresis loop for sample S3 is also observed, suggesting a more complex pore network. After treatment, isotherm shapes indicate minimal changes in adsorption behavior. PSDs were extracted using the density functional theory (DFT) with a slit-shaped model. Incremental pore volume curves of S2 (Figure 8c) and S3 (Figure 8d) show a main peak in the mesopore region (20–40 nm) and broader distribution for S3, with a larger fine-mesopore volume (2–20 nm) than S2. The increase in fine mesopores for S3 results in a larger BET surface area (Figure 8e). After treatment, no significant alterations in PSD or BET surface areas are observed. Sample S3 exhibits a slight decrease in mesopore volume followed by a minor increase in the fine-mesopore range, resulting in a slight decrease in surface area, but these differences are small and do not significantly impact cumulative pore volumes in the nanopore range.
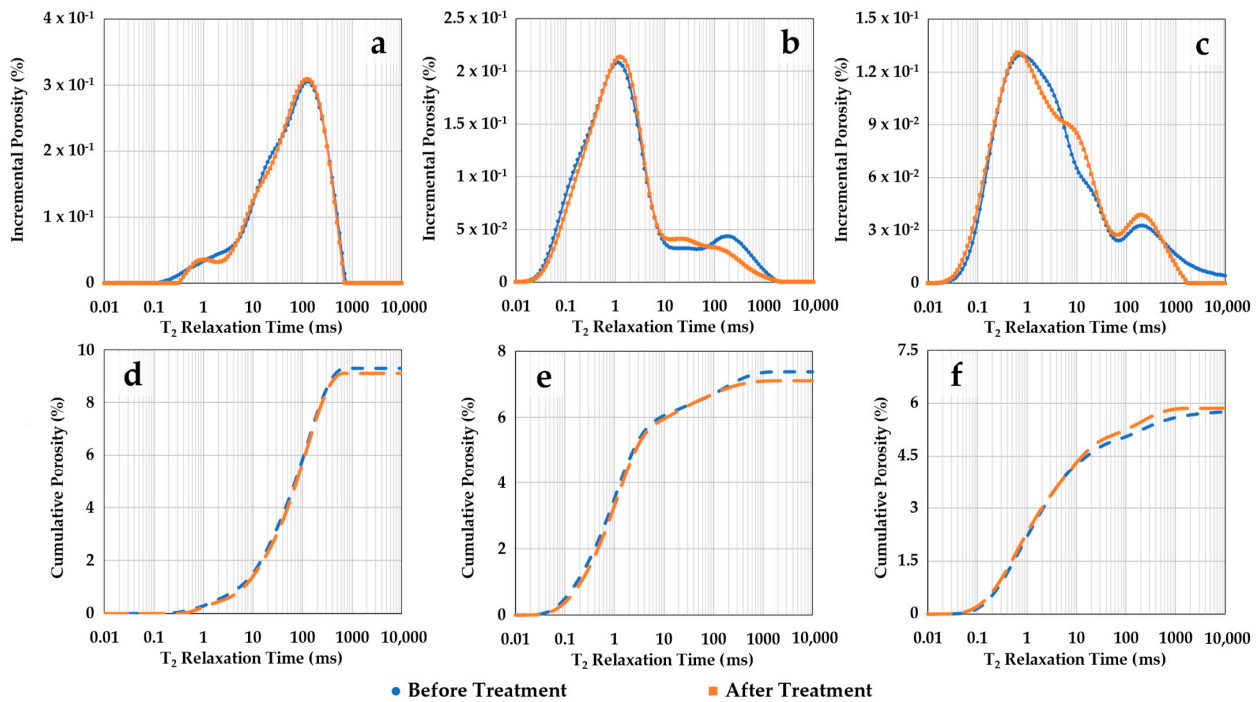
Figure 7. NMR porosities as function of T_2 relaxation time before and after scCO$_2$-enriched brine treatment. The incremental curves for samples S1, S2, and S3 are shown in (**a**–**c**), respectively. Their cumulative curves are sequentially represented in (**d**–**f**). Negligible alteration in the NMR porosity distributions is observed, aside from a small inflection around 1–20 ms for sample S3, which does not affect its cumulative porosity.
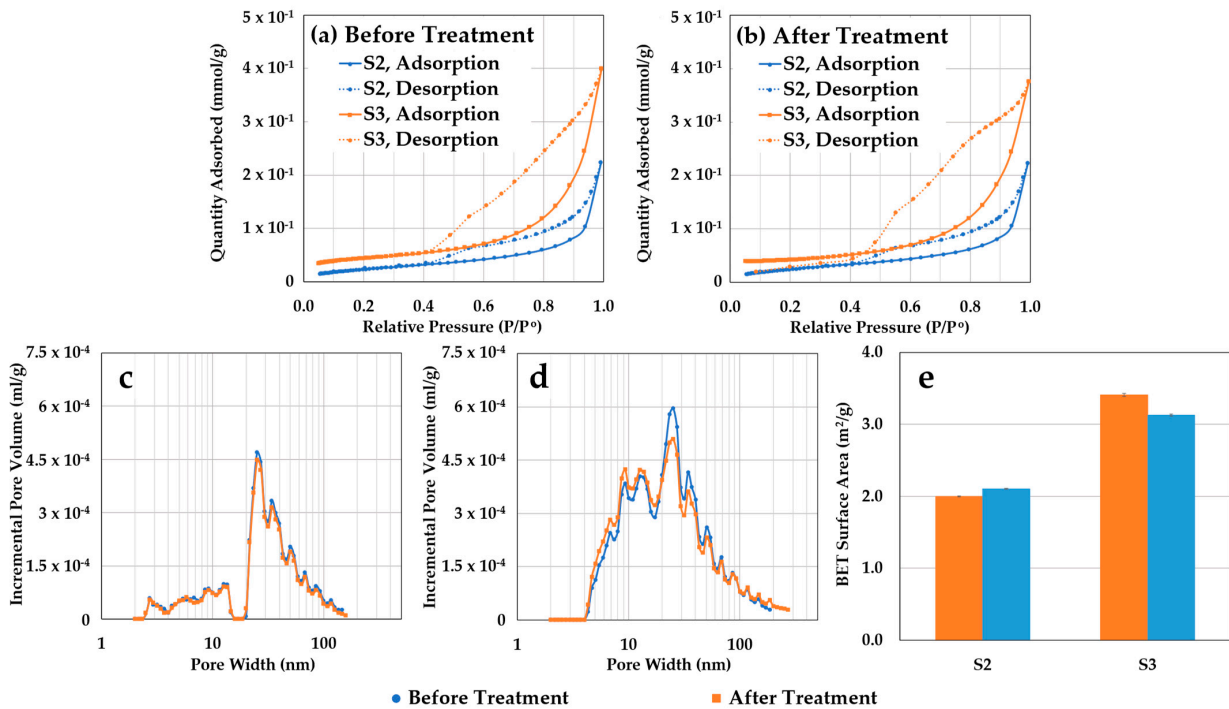
Figure 8. Isothermal N$_2$ adsorption results for the confining zone samples S2 and S3 before and after scCO$_2$-enriched brine treatment. (**a**) Before treatment, both samples exhibit type IV isotherms with

distinctive hysteresis loops and larger adsorption for sample S3. (**b**) After treatment, isotherm shapes remain stable, indicating minimal changes in adsorption behavior. (**c**) Incremental pore volume curves for S2 show a main peak in the mesopore region (20–40 nm) and constant PSD after treatment. (**d**) Incremental pore volume curves for S3 reveal a broader distribution, with a larger fine mesopore volume (2–20 nm) compared to S2, and slight alteration in PSD. (**e**) The increase in fine mesopores for S3 results in a larger BET surface area and slight alteration after treatment.

4. Discussion

Geochemical reactions arising from the dissolution of scCO$_2$ in brine have been experimentally proven to impact the microstructure of storage zones [89–91] and confining zones [60,69,73,92–98] even at short treatment times of typically few weeks. The impact on storage zones is commonly observed by dynamic injection flooding of scCO$_2$-enriched brine in limestone core samples. Significant dissolution (wormholes) has been reported on the inlet of the core plugs, followed by a small amount of precipitation in the far region. Although dynamic tests are important to evaluate geochemical effects in high flow regions (i.e., around injection wells), the extent of reactivity is prolonged because "fresh" reactant species (e.g., H$^+$) are continuously fed in open flow systems. On the other hand, geochemical alteration of confining zones is generally assessed by static scCO$_2$ treatments in closed systems conducted on crushed (micrometer size) samples. Significant geochemical reactivity has been reported by preferential dissolution (and precipitation) of carbonate minerals, which impact pore size distributions. However, the ultra-low transport properties of nanoporous confining zones imply concentration profiles of reactant species (e.g., H$^+$) across the samples [113,114]. Such concentration profiles favor surface reactivity and augment reactions on crushed samples due to their higher specific surface areas as compared to core plugs. In addition, the brine/rock volume ratio and brine composition selected in experiments can also impact reactivity [94,95,99]. When a large brine/rock volume ratio or calcium-depleted brines are used in closed systems, a higher Ca^{2+} uptake from calcite dissolution is needed before the reaction ceases (pH~4.5–5). Nonetheless, reactive transport studies show that geochemical reactions driven by diffusion in nanoporous confining zones are expected to impact properties on the scale of hundreds to thousands of years [80]. A strategy to overcome long experimental times is the combination of quantitative tools that can simultaneously resolve such alterations at the surface level up to the nanometer, micrometer, and millimeter depth of invasion.

Here, the impact of geochemical reactions is quantified by both surface characterization and three different PSD measurements conducted on thin disk samples. SEM/EDS images reveal surface dissolution of calcite grains after treatment, while other potentially reactive minerals remain unaltered (e.g., dolomite, clays, pyrite). Although surface reactivity occurred, little alteration is seen on the PSDs obtained with MICP, NMR, and N$_2$ adsorption after treatment. Minor changes were consistently observed in sample S3: MICP indicated a small amplitude increase in the 100–1000 nm range, followed by an amplitude drop in the main peak at 1–10 nm; the NMR T$_2$ spectrum exhibited a small inflection around 1–20 ms; and N$_2$ adsorption showed a slight increase in the main peak at 20–40 nm followed by small reduction at fine mesopores (1–20 nm). Combined with SEM/EDS data, it is understood that the small changes in PSD of sample S3 could be indicative of the surface dissolution of calcite. Potential precipitation below the surface that can cause a reduction in micropore volume is possible due to a local increase in the concentration of Ca^{2+} driven by surface dissolution (Equation (6)). Based on this study's experimental conditions, the geochemical reactivity on the confining zone samples preferentially occurs at the surface and does not impact pore size distributions or porosities at a core scale.

The alteration in surface mineralogy by calcite dissolution could change surface hydrophilicity and impact the wettability and hence the trapping mechanisms in the scCO$_2$–brine–rock system. However, the fluid-equilibrated scCO$_2$–brine–rock contact angles (θ) reported here are little influenced by the reactivity occurring at the surface. The rocks studied here maintain their water-wettability at high-pressure conditions (~20 MPa) and even after moderate or strong surface reactivity. Calcite dissolution in the forms of etching and pitting could locally increase the surface roughness (Figure 3f), which has been found to decrease θ in hydrophilic surfaces of pure minerals (e.g., quartz, calcite) [51,56]. In fine-grained heterogeneous surfaces such as confining zones, the large difference in scale between the static scCO$_2$ bubble (millimeter size) and grain size (micrometer to nanometer) accounts for small roughness changes due to dissolution that could impact the contact angle. It is also found that using NMR to assess wettability alteration due to dissolution in nanoporous media [115,116] is experimentally challenging because the geochemical reactivity shown here does not appear to influence the surface relaxivity of the bulk rock (Figure 8).

The microscopic displacement efficiency and primary trapping mechanisms during scCO$_2$ storage are tied to capillary properties including interfacial tension (IFT), wettability, and pore size. Miller, et al. [99] showed that the aqueous geochemistry of high-concentration analytes that could impact the IFT remains fairly constant during scCO$_2$ treatment. Therefore, changes in brine ionic concentration due to dissolution or precipitation of species are not expected to alter the scCO$_2$–brine–rock IFT. Regarding wettability, this work demonstrated that contact angles are barely affected by induced geochemical reactions in scCO$_2$–brine–rock systems. With the contact angles reported here and knowledge of the scCO$_2$–brine IFT at subsurface conditions, Hg–air capillary pressure measurements can be converted to subsurface scCO$_2$–brine conditions

:

$$P_{c,scCO_2:H_2O} = \frac{\gamma_{scCO_2:H_2O} \times \cos\theta_{scCO_2:H_2O}}{\gamma_{Hg:air} \times \cos\theta_{Hg:air}} \times P_{c,Hg:air} \approx \left| \frac{\left(\frac{27\ mN}{m}\right) \times \cos(35°)}{\left(\frac{485\ mN}{m}\right) \times \cos(130°)} \right| \times P_{c,Hg:air} \approx 0.07 P_{c,Hg:air} \tag{8}$$

assuming a scCO$_2$–brine IFT for this work experimental conditions of 27 mN/m [23], θ of the sample S3 (35°), Hg–air θ of 130°, and surface tension of 485 mN/m (laboratory conditions). Equation (8) indicates that the scCO$_2$–brine capillary pressure (Pc) at subsurface conditions for the confining zone S3 is about ~14 times smaller than laboratory Hg–air Pc.

During the short-term experiments, the predominant geochemical reactions were directed toward altering carbonate minerals, leaving the capillary properties of the quartz-rich sandstone largely unaffected within the experimental duration. The sandstone exhibited minimal reactivity, which aligns with findings in similar studies conducted over comparable timeframes and under analogous experimental conditions [91,117–120]. It is conceivable that extended treatment periods (0.5–1.5 years) might reveal some level of reactivity with quartz [69,104], although this is less likely to substantially influence surface wettability, as suggested by the consistently unaltered contact angles reported in this study.

Conversely, the main implication of such reactions for the capillary displacement of the confining zone appears to be an increase in pore size at the surface due to calcite dissolution followed by possible precipitation. The preferential reactivity of confining zones toward carbonate minerals agrees with literature experiments on crushed samples conducted in similar timescales [92,94,95,98,99]. Although these experiments also reported alterations in pore size distributions (PSDs) of crushed samples, we observed that the PSDs of intact samples obtained with three different methods remained unaltered. It is understood that the propagation of the geochemical reactions is controlled not only by mineralogy but experimental conditions (dynamic vs static exposure, water/rock brine ratio) as well as surface area and matrix transport properties. Therefore, short-term geochemical reactions do not seem to significantly impact the capillary displacement in quartz-rich storage reservoirs or primary capillary trapping mechanisms in either siltstone or mudstone confining zones in the condition studied.

5. Conclusions

In this experimental study, sandstone (storage zone), clay-rich siltstone, and carbonate-rich mudstone (confining zones) thin disk samples were treated under a scCO$_2$-enriched brine condition (10:1 brine/rock volume ratio) for 21 days at 20.7 MPa and 65 °C using a 2.5 wt.% KCl brine solution. Before and after treatment, geochemical alterations were assessed at the surface level using scanning electron microscopy (SEM) coupled with energy-dispersive X-ray spectroscopy (EDS) and X-ray fluorescence (XRF). Fluid-equilibrated scCO$_2$–brine–rock contact angle measurements were conducted to monitor wettability changes using the captive-bubble method. Pore size alterations were determined using mercury injection capillary pressure (MICP), nuclear magnetic resonance (NMR), and isothermal N$_2$ adsorption. The main conclusions of this work are as follows:

- Carbonate minerals preferentially react at the surface level in the form of calcite dissolution, while other potentially reactive minerals such as feldspars, clays, dolomite, and pyrite remain preserved. A reduction in the relative content of calcium oxide (CaO) from 55 wt.% to 14 wt.% is observed at the surface.
- Before treatment, fluid-equilibrated scCO$_2$–brine–rock contact angles are comparable with the literature values for storage and confining zones. Contact angles of $42 \pm 1°$, $37 \pm 1°$, and $35 \pm 2°$ were determined for sandstone, siltstone, and mudstone, respectively. After treatment, negligible alteration in the contact angles is observed, despite surface dissolution in the forms of etching and pitting for the carbonate-rich mudstone (S3). The rocks studied here maintain their water-wettability after geochemical reactivity and at elevated pressures (~20 MPa).
- Although reactions are observed at the surface, the pore size distributions (PSDs) of the thin disk samples obtained with three different methods (MICP, NMR, and N$_2$ adsorption) show

little alteration. Minor changes are consistently observed for the carbonate-rich mudstone (S3). Coupled with SEM/EDS images, these changes could be indicative of surface dissolution of calcite followed by possible precipitation. Overall, the short-term geochemical reactions observed here did not significantly impact the cumulative porosities or PSD of the three samples.

Our research demonstrates that short-term geochemical reactions do not substantially impact the capillary displacement mechanism in the studied quartz-rich sandstone storage reservoirs and siltstone/mudstone confining zones. These findings contribute valuable insights into the behavior of scCO₂– brine–rock systems and highlight the preservation of rock properties under the conditions examined.

References

1. Davis, S.J.; Lewis, N.S.; Shaner, M.; Aggarwal, S.; Arent, D.; Azevedo, I.L.; Benson, S.M.; Bradley, T.; Brouwer, J.; Chiang, Y.-M.; et al. Net-zero emissions energy systems. *Science* **2018**, *360*, eaas9793. [CrossRef] [PubMed]
2. Zhao, H. *Phase Equilibria in CO₂-Brine System for CO₂ Storage*; ProQuest Dissertations Publishing: Ann Arbor, MI, USA, 2014.
3. Heinemann, N.; Wilkinson, M.; Pickup, G.E.; Haszeldine, R.S.; Cutler, N.A. CO₂ storage in the offshore UK Bunter Sandstone Formation. *Int. J. Greenh. Gas Control* **2012**, *6*, 210–219. [CrossRef]
4. Medici, G.; West, L.J. Reply to discussion on 'Review of groundwater flow and contaminant transport modelling approaches for the Sherwood Sandstone aquifer, UK insights from analogous successions worldwide' by Medici and West (QJEGH, 55, qjegh2021-176). *Q. J. Eng. Geol. Hydrogeol.* **2023**, *56*, qjegh2022-097. [CrossRef]
5. Zhang, C.P.; Ranjith, P.G.; Perera, M.S.A.; Zhao, J.; Zhang, D.; Wanniarachchi, W.A.M. A novel approach to precise evaluation of carbon dioxide flow behaviour in siltstone under tri-axial drained conditions. *J. Nat. Gas Sci. Eng.* **2016**, *34*, 331–340. [CrossRef]
6. Jayasekara, D.W.; Ranjith, P.G.; Wanniarachchi, W.A.M.; Rathnaweera, T.D.; Chaudhuri, A. Effect of salinity on supercritical CO₂ permeability of caprock in deep saline aquifers: An experimental study. *Energy* **2020**, *191*, 116486. [CrossRef]
7. Lima, V.d.; Einloft, S.; Ketzer, J.M.; Jullien, M.; Bildstein, O.; Petronin, J.-C. CO₂ Geological storage in saline aquifers: Paraná Basin caprock and reservoir chemical reactivity. *Energy Procedia* **2011**, *4*, 5377–5384. [CrossRef]
8. Shi, J.-Q.; Sinayuc, C.; Durucan, S.; Korre, A. Assessment of carbon dioxide plume behaviour within the storage reservoir and the lower caprock around the KB-502 injection well at In Salah. *Int. J. Greenh. Gas Control* **2012**, *7*, 115–126. [CrossRef]
9. Zhang, K.; Sang, S.; Zhou, X.; Liu, C.; Ma, M.; Niu, Q. Influence of supercritical CO₂-H₂O-caprock interactions on the sealing capability of deep coal seam caprocks related to CO₂ geological storage: A case study of the silty mudstone caprock of coal seam no. 3 in the Qinshui Basin, China. *Int. J. Greenh. Gas Control* **2021**, *106*, 103282. [CrossRef]
10. Lu, J.; Wilkinson, M.; Haszeldine, R.S.; Fallick, A.E. Long-term performance of a mudrock seal in natural CO₂ storage. *Geology* **2009**, *37*, 35–38. [CrossRef]
11. Lake, L.W. *Enhanced Oil Recovery*; Prentice Hall: Saddle River, NJ, USA, 1989.
12. Bachu, S.; Bonijoly, D.; Bradshaw, J.; Burruss, R.; Holloway, S.; Christensen, N.P.; Mathiassen, O.M. CO₂ storage capacity estimation: Methodology and gaps. *Int. J. Greenh. Gas Control* **2007**, *1*, 430–443. [CrossRef]
13. Bachu, S. Review of CO₂ storage efficiency in deep saline aquifers. *Int. J. Greenh. Gas Control* **2015**, *40*, 188–202. [CrossRef]
14. Al Hameli, F.; Belhaj, H.; Al Dhuhoori, M. CO₂ Sequestration Overview in Geological Formations: Trapping Mechanisms Matrix Assessment. *Energies* **2022**, *15*, 7805. [CrossRef]
15. Ajayi, T.; Gomes, J.S.; Bera, A. A review of CO₂ storage in geological formations emphasizing modeling, monitoring and capacity estimation approaches. *Pet. Sci.* **2019**, *16*, 1028–1063. [CrossRef]
16. Kaszuba, J.; Yardley, B.; Andreani, M. Experimental perspectives of mineral dissolution and precipitation due to carbon dioxide-water-rock interactions. *Rev. Mineral. Geochem.* **2013**, *77*, 153–188. [CrossRef]
17. Song, J.; Zhang, D. Comprehensive Review of Caprock-Sealing Mechanisms for Geologic Carbon Sequestration. *Environ. Sci. Technol.* **2013**, *47*, 9–22. [CrossRef] [PubMed]

18.　Abidoye, L.K.; Khudaida, K.J.; Das, D.B. Geological Carbon Sequestration in the Context of Two-Phase Flow in Porous Media: A Review. *Crit. Rev. Environ. Sci. Technol.* **2015**, *45*, 1105–1147. [CrossRef]

19.　Cai, J.; Jin, T.; Kou, J.; Zou, S.; Xiao, J.; Meng, Q. Lucas–Washburn Equation-Based Modeling of Capillary-Driven Flow in Porous Systems. *Langmuir* **2021**, *37*, 1623–1636. [CrossRef]

20.　Behroozi, F. A Fresh Look at the Young-Laplace Equation and Its Many Applications in Hydrostatics. *Phys. Teach.* **2022**, *60*, 358–361. [CrossRef]

21.　Chiquet, P.; Daridon, J.-L.; Broseta, D.; Thibeau, S. CO_2/water interfacial tensions under pressure and temperature conditions of CO_2 geological storage. *Energy Convers. Manag.* **2007**, *48*, 736–744. [CrossRef]

22.　Van der Meer, L.G.H.; Hofstee, C.; Orlic, B. The fluid flow consequences of CO_2 migration from 1000 to 600 metres upon passing the critical conditions of CO_2. *Energy Procedia* **2009**, *1*, 3213–3220. [CrossRef]

23.　Chalbaud, C.; Robin, M.; Lombard, J.M.; Martin, F.; Egermann, P.; Bertin, H. Interfacial tension measurements and wettability evaluation for geological CO_2 storage. *Adv. Water Resour.* **2009**, *32*, 98–109. [CrossRef]

24.　Bikkina, P.K.; Shoham, O.; Uppaluri, R. Equilibrated Interfacial Tension Data of the CO_2–Water System at High Pressures and Moderate Temperatures. *J. Chem. Eng. Data* **2011**, *56*, 3725–3733. [CrossRef]

25.　Li, X.; Boek, E.; Maitland, G.C.; Trusler, J.P.M. Interfacial Tension of (Brines + CO_2): (0.864 NaCl + 0.136 KCl) at Temperatures between (298 and 448) K, Pressures between (2 and 50) MPa, and Total Molalities of (1 to 5) mol·kg^{-1}. *J. Chem. Eng. Data* **2012**, *57*, 1078–1088. [CrossRef]

26.　Pereira, L.M.C.; Chapoy, A.; Burgass, R.; Oliveira, M.B.; Coutinho, J.A.P.; Tohidi, B. Study of the impact of high temperatures and pressures on the equilibrium densities and interfacial tension of the carbon dioxide/water system. *J. Chem. Thermodyn.* **2016**, *93*, 404–415. [CrossRef]

27.　Hebach, A.; Oberhof, A.; Dahmen, N.; Kögel, A.; Ederer, H.; Dinjus, E. Interfacial Tension at Elevated PressuresMeasurements and Correlations in the Water + Carbon Dioxide System. *J. Chem. Eng. Data* **2002**, *47*, 1540–1546. [CrossRef]

28.　Aggelopoulos, C.A.; Robin, M.; Perfetti, E.; Vizika, O. CO_2/$CaCl_2$ solution interfacial tensions under CO_2 geological storage conditions: Influence of cation valence on interfacial tension. *Adv. Water Resour.* **2010**, *33*, 691–697. [CrossRef]

29.　Aggelopoulos, C.A.; Robin, M.; Vizika, O. Interfacial tension between CO_2 and brine (NaCl + $CaCl_2$) at elevated pressures and temperatures: The additive effect of different salts. *Adv. Water Resour.* **2011**, *34*, 505–511. [CrossRef]

30.　Bennion, B.; Bachu, S. Relative Permeability Characteristics for Supercritical CO_2 Displacing Water in a Variety of Potential Sequestration Zones in the Western Canada Sedimentary Basin. In Proceedings of the SPE Annual Technical Conference and Exhibition, Dallas, TX, USA, 9–12 October 2005.

31.　Chiquet, P.; Broseta, D.; Thibeau, S. Wettability alteration of caprock minerals by carbon dioxide. *Geofluids* **2007**, *7*, 112–122. [CrossRef]

32.　Yang, D.; Gu, Y.; Tontiwachwuthikul, P. Wettability Determination of the Reservoir Brine−Reservoir Rock System with Dissolution of CO_2 at High Pressures and Elevated Temperatures. *Energy Fuels* **2008**, *22*, 504–509. [CrossRef]

33.　Espinoza, D.N.; Santamarina, J.C. Water-CO_2-mineral systems: Interfacial tension, contact angle, and diffusion-Implications to CO_2 geological storage. *Water Resour. Res.* **2010**, *46*. [CrossRef]

34.　Bikkina, P. Contact angle measurements of CO_2-water-quartz/calcite systems in the perspective of carbon sequestration. *Int. J. Greenh. Gas Control* **2011**, *5*, 1259–1271. [CrossRef]

35.　Mills, J.; Riazi, M.; Sohrabi, M. *Wettability of Common Rock-Forming Minerals in a CO_2-Brine System at Reservoir Conditions*; Society of Core Analysts Fredericton, Canada: Fredericton, NJ, Canada, 2011.

36.　Tonnet, N.; Mouronval, G.; Chiquet, P.; Broseta, D. Petrophysical assessment of a carbonate-rich caprock for CO_2 geological storage purposes. *Energy Procedia* **2011**, *4*, 5422–5429. [CrossRef]

37.　Broseta, D.; Tonnet, N.; Shah, V. Are rocks still water-wet in the presence of dense CO_2 or H_2S? *Geofluids* **2012**, *12*, 280–294. [CrossRef]

38.　Jung, J.-W.; Jiamin, W.A.N. Supercritical CO_2 and Ionic Strength Effects on Wettability of Silica Surfaces: Equilibrium Contact Angle Measurements. *Energy Fuels* **2012**, *26*, 6053–6059. [CrossRef]

39.　Kim, Y.; Wan, J.; Kneafsey, T.J.; Tokunaga, T.K. Dewetting of Silica Surfaces upon Reactions with Supercritical CO_2 and Brine: Pore-Scale Studies in Micromodels. *Environ. Sci. Technol.* **2012**, *46*, 4228–4235. [CrossRef]

40.　Farokhpoor, R.; Bjørkvik, B.J.A.; Lindeberg, E.; Torsæter, O. CO_2 Wettability Behavior During CO_2 Sequestration in Saline Aquife—An Experimental Study on Minerals Representing Sandstone and Carbonate. *Energy Procedia* **2013**, *37*, 5339–5351. [CrossRef]

41.　Saraji, S.; Goual, L.; Piri, M.; Plancher, H. Wettability of Supercritical Carbon Dioxide/Water/Quartz Systems: Simultaneous Measurement of Contact Angle and Interfacial Tension at Reservoir Conditions. *Langmuir* **2013**, *29*, 6856–6866. [CrossRef] [PubMed]

42.　Wang, S.; Edwards, I.M.; Clarens, A.F. Wettability Phenomena at the CO_2–Brine–Mineral Interface: Implications for Geologic Carbon Sequestration. *Environ. Sci. Technol.* **2013**, *47*, 234–241. [CrossRef]

43.　Andrew, M.; Bijeljic, B.; Blunt, M.J. Pore-scale contact angle measurements at reservoir conditions using X-ray microtomography. *Adv. Water Resour.* **2014**, *68*, 24–31. [CrossRef]

44.　Iglauer, S.; Salamah, A.; Sarmadivaleh, M.; Liu, K.; Phan, C. Contamination of silica surfaces: Impact on water-CO_2-quartz and glass contact angle measurements. *Int. J. Greenh. Gas Control* **2014**, *22*, 325–328. [CrossRef]

45. Kaveh, N.S.; Rudolph, E.S.J.; van Hemert, P.; Rossen, W.R.; Wolf, K.H. Wettability Evaluation of a CO_2/Water/Bentheimer Sandstone System: Contact Angle, Dissolution, and Bubble Size. *Energy Fuels* **2014**, *28*, 4002–4020. [CrossRef]

46. Saraji, S.; Piri, M.; Goual, L. The effects of SO_2 contamination, brine salinity, pressure, and temperature on dynamic contact angles and interfacial tension of supercritical CO_2/brine/quartz systems. *Int. J. Greenh. Gas Control* **2014**, *28*, 147–155. [CrossRef]

47. Al-Yaseri, A.; Sarmadivaleh, M.; Saeedi, A.; Lebedev, M.; Barifcani, A.; Iglauer, S. N_2 + CO_2 + NaCl brine interfacial tensions and contact angles on quartz at CO_2 storage site conditions in the Gippsland basin, Victoria/Australia. *J. Pet. Sci. Eng.* **2015**, *129*, 58–62. [CrossRef]

48. Chaudhary, K.; Guiltinan, E.J.; Cardenas, M.B.; Maisano, J.A.; Ketcham, R.A.; Bennett, P.C. Wettability measurement under high P-T conditions using X-ray imaging with application to the brine-supercritical CO_2 system. *Geochem. Geophys. Geosystems G3* **2015**, *16*, 2858–2864. [CrossRef]

49. Iglauer, S.; Al-Yaseri, A.Z.; Rezaee, R.; Lebedev, M. CO_2 wettability of caprocks: Implications for structural storage capacity and containment security. *Geophys. Res. Lett.* **2015**, *42*, 9279–9284. [CrossRef]

50. Liu, Y.; Mutailipu, M.; Jiang, L.; Zhao, J.; Song, Y.; Chen, L. Interfacial tension and contact angle measurements for the evaluation of CO_2-brine two-phase flow characteristics in porous media. *Environ. Prog. Sustain. Energy* **2015**, *34*, 1756–1762. [CrossRef]

51. Al-Yaseri, A.Z.; Lebedev, M.; Barifcani, A.; Iglauer, S. Receding and advancing (CO_2 + brine + quartz) contact angles as a function of pressure, temperature, surface roughness, salt type and salinity. *J. Chem. Thermodyn.* **2016**, *93*, 416–423. [CrossRef]

52. Lv, P.; Liu, Y.; Jiang, L.; Song, Y.; Wu, B.; Zhao, J.; Zhang, Y. Experimental determination of wettability and heterogeneity effect on CO_2 distribution in porous media. *Greenh. Gases Sci. Technol.* **2016**, *6*, 401–415. [CrossRef]

53. Roshan, H.; Al-Yaseri, A.Z.; Sarmadivaleh, M.; Iglauer, S. On wettability of shale rocks. *J. Colloid. Interface Sci.* **2016**, *475*, 104–111. [CrossRef]

54. Shojai Kaveh, N.; Barnhoorn, A.; Wolf, K.H. Wettability evaluation of silty shale caprocks for CO_2 storage. *Int. J. Greenh. Gas Control* **2016**, *49*, 425–435. [CrossRef]

55. Al-Yaseri, A.Z.; Roshan, H.; Zhang, Y.; Rahman, T.; Lebedev, M.; Barifcani, A.; Iglauer, S. Effect of the Temperature on CO_2/Brine/Dolomite Wettability: Hydrophilic versus Hydrophobic Surfaces. *Energy Fuels* **2017**, *31*, 6329–6333. [CrossRef]

56. Arif, M.; Lebedev, M.; Barifcani, A.; Iglauer, S. CO_2 storage in carbonates: Wettability of calcite. *Int. J. Greenh. Gas Control* **2017**, *62*, 113–121. [CrossRef]

57. Botto, J.; Fuchs, S.J.; Fouke, B.W.; Clarens, A.F.; Freiburg, J.T.; Berger, P.M.; Werth, C.J. Effects of Mineral Surface Properties on Supercritical CO_2 Wettability in a Siliciclastic Reservoir. *Energy Fuels* **2017**, *31*, 5275–5285. [CrossRef]

58. Guiltinan, E.J.; Cardenas, M.B.; Bennett, P.C.; Zhang, T.; Espinoza, D.N. The effect of organic matter and thermal maturity on the wettability of supercritical CO_2 on organic shales. *Int. J. Greenh. Gas Control* **2017**, *65*, 15–22. [CrossRef]

59. Lv, P.; Liu, Y.; Wang, Z.; Liu, S.; Jiang, L.; Chen, J.; Song, Y. In Situ Local Contact Angle Measurement in a CO_2–Brine–Sand System Using Microfocused X-ray CT. *Langmuir* **2017**, *33*, 3358–3366. [CrossRef]

60. Qin, C.; Jiang, Y.; Luo, Y.; Xian, X.; Liu, H.; Li, Y. Effect of Supercritical Carbon Dioxide Treatment Time, Pressure, and Temperature on Shale Water Wettability. *Energy Fuels* **2017**, *31*, 493–503. [CrossRef]

61. Tudek, J.; Crandall, D.; Fuchs, S.; Werth, C.J.; Valocchi, A.J.; Chen, Y.; Goodman, A. In situ contact angle measurements of liquid CO_2, brine, and Mount Simon sandstone core using micro X-ray CT imaging, sessile drop, and Lattice Boltzmann modeling. *J. Pet. Sci. Eng.* **2017**, *155*. [CrossRef]

62. Alnili, F.; Al-Yaseri, A.; Roshan, H.; Rahman, T.; Verall, M.; Lebedev, M.; Sarmadivaleh, M.; Iglauer, S.; Barifcani, A. Carbon dioxide/brine wettability of porous sandstone versus solid quartz: An experimental and theoretical investigation. *J. Colloid. Interface Sci.* **2018**, *524*, 188–194. [CrossRef]

63. Pan, B.; Li, Y.; Wang, H.; Jones, F.; Iglauer, S. CO_2 and CH_4 Wettabilities of Organic-Rich Shale. *Energy Fuels* **2018**, *32*, 1914–1922. [CrossRef]

64. Prem, B.; Imran, S. Interfacial Tension and Contact Angle Data Relevant to Carbon Sequestration. In *Carbon Capture, Utilization and Sequestration*; Ramesh, K.A., Ed.; IntechOpen: Rijeka, Croatia, 2018; p. 10.

65. Arif, M.; Abu-Khamsin, S.A.; Iglauer, S. Wettability of rock/CO_2/brine and rock/oil/CO_2-enriched-brine systems:Critical parametric analysis and future outlook. *Adv. Colloid. Interface Sci.* **2019**, *268*, 91–113. [CrossRef]

66. Mutailipu, M.; Liu, Y.; Jiang, L.; Zhang, Y. Measurement and estimation of CO_2–brine interfacial tension and rock wettability under CO_2 sub- and super-critical conditions. *J. Colloid. Interface Sci.* **2019**, *534*, 605–617. [CrossRef] [PubMed]

67. Yekeen, N.; Padmanabhan, E.; Sevoo, T.A.L.; Kanesen, K.A.L.; Okunade, O.A. Wettability of rock/CO_2/brine systems: A critical review of influencing parameters and recent advances. *J. Ind. Eng. Chem.* **2020**, *88*, 1–28. [CrossRef]

68. Baban, A.; Al-Yaseri, A.; Keshavarz, A.; Amin, R.; Iglauer, S. CO_2—brine—sandstone wettability evaluation at reservoir conditions via Nuclear Magnetic Resonance measurements. *Int. J. Greenh. Gas Control* **2021**, *111*, 103435. [CrossRef]

69. Gholami, R.; Raza, A.; Andersen, P.; Escalona, A.; Cardozo, N.; Marín, D.; Sarmadivaleh, M. Long-term integrity of shaly seals in CO_2 geo-sequestration sites: An experimental study. *Int. J. Greenh. Gas Control* **2021**, *109*, 103370. [CrossRef]

70. Hashemi, L.; Glerum, W.; Farajzadeh, R.; Hajibeygi, H. Contact angle measurement for hydrogen/brine/sandstone system using captive-bubble method relevant for underground hydrogen storage. *Adv. Water Resour.* **2021**, *154*, 103964. [CrossRef]

71. Al-Yaseri, A.; Abbasi, G.R.; Yekeen, N.; Al-Shajalee, F.; Giwelli, A.; Xie, Q. Effects of cleaning process using toluene and acetone on water-wet-quartz/CO_2 and oil-wet-quartz/CO_2 wettability. *J. Pet. Sci. Eng.* **2022**, *208*, 109555. [CrossRef]

72. Baban, A.; Keshavarz, A.; Amin, R.; Iglauer, S. Impact of Wettability Alteration on CO_2 Residual Trapping in Oil-Wet Sandstone at Reservoir Conditions Using Nuclear Magnetic Resonance. *Energy Fuels* **2022**, *36*, 13722–13731. [CrossRef]

73. Qin, C.; Jiang, Y.; Zhou, J.; Zuo, S.; Chen, S.; Liu, Z.; Yin, H.; Li, Y. Influence of supercritical CO_2 exposure on water wettability of shale: Implications for CO_2 sequestration and shale gas recovery. *Energy* **2022**, *242*, 122551. [CrossRef]

74. Song, J.Y.; Jeong, Y.J.; Yun, T.S. Effects of Anisotropy and CO_2 Wettability on CO_2 Storage Capacity in Sandstone. *Geofluids* **2022**, *2022*, 5900255. [CrossRef]

75. Al-Khdheeawi, E.A.; Vialle, S.; Barifcani, A.; Sarmadivaleh, M.; Iglauer, S. Effect of wettability heterogeneity and reservoir temperature on CO_2 storage efficiency in deep saline aquifers. *Int. J. Greenh. Gas Control* **2018**, *68*, 216–229. [CrossRef]

76. Iglauer, S.; Pentland, C.H.; Busch, A. CO_2 wettability of seal and reservoir rocks and the implications for carbon geo-sequestration. *Water Resour. Res.* **2015**, *51*, 729–774. [CrossRef]

77. Rahman, T.; Lebedev, M.; Barifcani, A.; Iglauer, S. Residual trapping of supercritical CO_2 in oil-wet sandstone. *J. Colloid. Interface Sci.* **2016**, *469*, 63. [CrossRef]

78. Espinoza, D.N.; Santamarina, J.C. CO_2 breakthrough—Caprock sealing efficiency and integrity for carbon geological storage. *Int. J. Greenh. Gas Control* **2017**, *66*, 218–229. [CrossRef]

79. Stavropoulou, E.; Laloui, L. Evaluating CO_2 breakthrough in a shaly caprock material: A multi-scale experimental approach. *Sci. Rep.* **2022**, *12*, 10706. [CrossRef]

80. Gaus, I.; Azaroual, M.; Czernichowski-Lauriol, I. Reactive transport modelling of the impact of CO_2 injection on the clayey cap rock at Sleipner (North Sea). *Chem. Geol.* **2005**, *217*, 319–337. [CrossRef]

81. Gaus, I. Role and impact of CO_2–rock interactions during CO_2 storage in sedimentary rocks. *Int. J. Greenh. Gas Control* **2010**, *4*, 73–89. [CrossRef]

82. Rosenbauer, R.J.; Koksalan, T.; Palandri, J.L. Experimental investigation of CO_2-brine-rock interactions at elevated temperature and pressure: Implications for CO_2 sequestration in deep-saline aquifers. *Fuel Process. Technol.* **2005**, *86*, 1581–1597. [CrossRef]

83. Espinoza, D.N.; Kim, S.H.; Santamarina, J.C. CO_2 geological storage—Geotechnical implications. *KSCE J. Civ. Eng.* **2011**, *15*, 707–719. [CrossRef]

84. Palandri, J.L.; Kharaka, Y.K. *A Compilation of Rate Parameters of Water—Mineral Interaction Kinetics for Application to Geochemical Modeling*; U.S. Geological Survey: Reston, VA, USA, 2004.

85. Pokrovsky, O.S.; Golubev, S.V.; Schott, J.; Castillo, A. Calcite, dolomite and magnesite dissolution kinetics in aqueous solutions at acid to circumneutral pH, 25 to 150 °C and 1 to 55 atm pCO$_2$: New constraints on CO_2 sequestration in sedimentary basins. *Chem. Geol.* **2009**, *260*, 317. [CrossRef]

86. Golubev, S.V.; Bénézeth, P.; Schott, J.; Dandurand, J.L.; Castillo, A. Siderite dissolution kinetics in acidic aqueous solutions from 25 to 100 °C and 0 to 50 atm pCO$_2$. *Chem. Geol.* **2009**, *265*, 13–19. [CrossRef]

87. Dresel, P.E. The Dissolution Kinetics of Siderite and Its Effect on Acid Mine Drainage. Ph.D. Thesis, The Pennsylvania State University, State College, PA, USA, 1989.

88. Gunter, W.D.; Wiwehar, B.; Perkins, E.H. Aquifer disposal of CO_2-rich greenhouse gases: Extension of the time scale of experiment for CO_2-sequestering reactions by geochemical modelling. *Mineral. Petrol.* **1997**, *59*, 121–140. [CrossRef]

89. Seyyedi, M.; Mahmud, H.K.B.; Verrall, M.; Giwelli, A.; Esteban, L.; Ghasemiziarani, M.; Clennell, B. Pore Structure Changes Occur During CO_2 Injection into Carbonate Reservoirs. *Sci. Rep.* **2020**, *10*, 3624. [CrossRef]

90. Wang, H.; Alvarado, V.; Smith, E.R.; Kaszuba, J.P.; Bagdonas, D.A.; McLaughlin, J.F.; Quillinan, S.A. Link Between CO_2-Induced Wettability and Pore Architecture Alteration. *Geophys. Res. Lett.* **2020**, *47*. [CrossRef]

91. Kim, K.; Kundzicz, P.M.; Makhnenko, R.Y. Effect of CO_2 Injection on the Multiphase Flow Properties of Reservoir Rock. *Transp. Porous Media* **2023**, *147*, 429–461. [CrossRef]

92. Mouzakis, K.M.; Navarre-Sitchler, A.K.; Rother, G.; Bañuelos, J.L.; Wang, X.; Kaszuba, J.P.; Heath, J.E.; Miller, Q.R.S.; Alvarado, V.; McCray, J.E. Experimental Study of Porosity Changes in Shale Caprocks Exposed to CO_2-Saturated Brines I: Evolution of Mineralogy, Pore Connectivity, Pore Size Distribution, and Surface Area. *Environ. Eng. Sci.* **2016**, *33*, 725–735. [CrossRef]

93. Pan, Y.; Hui, D.; Luo, P.; Zhang, Y.; Sun, L.; Wang, K. Experimental Investigation of the Geochemical Interactions between Supercritical CO_2 and Shale: Implications for CO_2 Storage in Gas-Bearing Shale Formations. *Energy Fuels* **2018**, *32*, 1963–1978. [CrossRef]

94. Sanguinito, S.; Goodman, A.; Tkach, M.; Kutchko, B.; Culp, J.; Natesakhawat, S.; Fazio, J.; Fukai, I.; Crandall, D. Quantifying dry supercritical CO_2-induced changes of the Utica Shale. *Fuel* **2018**, *226*, 54–64. [CrossRef]

95. Goodman, A.; Sanguinito, S.; Tkach, M.; Natesakhawat, S.; Kutchko, B.; Fazio, J.; Cvetic, P. Investigating the role of water on CO_2-Utica Shale interactions for carbon storage and shale gas extraction activities—Evidence for pore scale alterations. *Fuel* **2019**, *242*, 744–755. [CrossRef]

96. Fatah, A.; Mahmud, H.B.; Bennour, Z.; Hossain, M.; Gholami, R. Effect of supercritical CO_2 treatment on physical properties and functional groups of shales. *Fuel* **2021**, *303*, 121310. [CrossRef]

97. Medina, B.X.; Kohli, A.; Kovscek, A.R.; Alvarado, V. Effects of Supercritical CO_2 Injection on the Shale Pore Structures and Mass Transport Rates. *Energy Fuels* **2023**, *37*, 1151–1168. [CrossRef]

98. Wang, S.; Zhou, S.; Pan, Z.; Elsworth, D.; Yan, D.; Wang, H.; Liu, D.; Hu, Z. Response of pore network fractal dimensions and gas adsorption capacities of shales exposed to supercritical CO_2: Implications for CH_4 recovery and carbon sequestration. *Energy Rep.* **2023**, *9*, 6461–6485. [CrossRef]

99. Miller, Q.R.S.; Wang, X.; Kaszuba, J.P.; Mouzakis, K.M.; Navarre-Sitchler, A.K.; Alvarado, V.; McCray, J.E.; Rother, G.; Bañuelos, J.L.; Heath, J.E. Experimental Study of Porosity Changes in Shale Caprocks Exposed to Carbon Dioxide-Saturated Brine II: Insights from Aqueous Geochemistry. *Environ. Eng. Sci.* **2016**, *33*, 736–744. [CrossRef]

100. Cruz, F.; Tinni, A.; Brackeen, S.; Sondergeld, C.; Rai, C. Impact of Capillary Pressure on Total Porosity in Unconventional Shales. In Proceedings of the SPE/AAPG/SEG Unconventional Resources Technology Conference, Online, 20–22 July 2020.

101. Sondergeld, C.H.; Rai, C.S. A New Exploration Tool: Quantitative Core Characterization. In *Experimental Techniques in Mineral and Rock Physics: The Schreiber Volume*; Liebermann, R.C., Sondergeld, C.H., Eds.; Birkhäuser Basel: Basel, Switzerland, 1994; pp. 249–268.

102. Ballard, B. Quantitative Mineralogy of Reservoir Rocks Using Fourier Transform Infrared Spectroscopy. In Proceedings of the SPE Annual Technical Conference and Exhibition, Anaheim, CA, USA, 1 January 2007; p. 8.

103. Curtis, M.; Mamoudou, S.; Cruz, F.; Dang, S.; Rai, C.; Devegowda, D. Effects of CO_2 Exposure on Unconventional Reservoir Rock Microstructure. In Proceedings of the SPE/AAPG/SEG Unconventional Resources Technology Conference, Denver, CO, USA, 13–15 June 2023.

104. Rathnaweera, T.D.; Ranjith, P.G.; Perera, M.S.A. Experimental investigation of geochemical and mineralogical effects of CO_2 sequestration on flow characteristics of reservoir rock in deep saline aquifers. *Sci. Rep.* **2016**, *6*, 19362. [CrossRef] [PubMed]

105. Sokama-Neuyam, Y.A.; Boakye, P.; Aggrey, W.N.; Obeng, N.O.; Adu-Boahene, F.; Woo, S.H.; Ursin, J.R. Theoretical Modeling of the Impact of Salt Precipitation on CO_2 Storage Potential in Fractured Saline Reservoirs. *ACS Omega* **2020**, *5*, 14776–14785. [CrossRef]

106. Vilarrasa, V.; Rutqvist, J. Thermal effects on geologic carbon storage. *Earth-Sci. Rev.* **2017**, *165*, 245–256. [CrossRef]

107. Comisky, J.T.; Santiago, M.; McCollom, B.; Buddhala, A.; Newsham, K.E. Sample Size Effects on the Application of Mercury Injection Capillary Pressure for Determining the Storage Capacity of Tight Gas and Oil Shales. In Proceedings of the Canadian Unconventional Resources Conference, Calgary, AB, Canada, 1 January 2011; p. 23.

108. Wang, R.; Sang, S.; Zhu, D.; Liu, S.; Yu, K. Pore characteristics and controlling factors of the Lower Cambrian Hetang Formation shale in Northeast Jiangxi, China. *Energy Explor. Exploit.* **2017**, *36*, 43–65. [CrossRef]

109. Tian, Y.; Chen, Q.; Yan, C.; Deng, H.; He, Y. Classification of Adsorption Isotherm Curves for Shale Based on Pore Structure. *Petrophysics* **2020**, *61*, 417–433. [CrossRef]

110. Fuhua, S.; Ke, M.; Yanming, Z.H.U.; Meng, W.; Xin, T.; Yang, W.; Haitao, G.A.O.; Guangjun, F.; Wentian, M.I. Pore structure, adsorption capacity and their controlling factors of shale in complex structural area. *Méitàn Kēxué Jìshù* **2023**, *51*, 269–282. [CrossRef]

111. Thommes, M.; Kaneko, K.; Neimark, A.V.; Olivier, J.P.; Rodriguez-Reinoso, F.; Rouquerol, J.; Sing, K.S.W. Physisorption of gases, with special reference to the evaluation of surface area and pore size distribution (IUPAC Technical Report). *Pure Appl. Chem.* **2015**, *87*, 1051–1069. [CrossRef]

112. Sing, K.S.W. Reporting physisorption data for gas/solid systems with special reference to the determination of surface area and porosity (Recommendations 1984). *Pure Appl. Chem.* **1985**, *57*, 603–619. [CrossRef]

113. Dang, S.; Mukherjee, S.; Sondergeld, C.; Rai, C. Measurement of Effective Tortuosity in Unconventional Tight Rock using Nuclear Magnetic Resonance. In Proceedings of the SPE/AAPG/SEG Unconventional Resources Technology Conference, Online, 26–28 July 2021.

114. Odiachi, J.; Cruz, F.; Tinni, A. Diffusional and Electrical Tortuosity in Unconventional Shale Reservoirs. In Proceedings of the SPE Annual Technical Conference and Exhibition, Houston, TX, USA, 3–5 October 2022.

115. Tinni, A.; Odusina, E.; Sulucarnain, I.; Sondergeld, C.; Rai, C.S. Nuclear-Magnetic-Resonance Response of Brine, Oil, and Methane in Organic-Rich Shales. *SPE Reserv. Eval. Eng.* **2015**, *18*, 400–406. [CrossRef]

116. Mukherjee, S.; Dang, S.T.; Rai, C.; Sondergeld, C. Revisiting the Concept of Wettability for Organic-Rich Tight Rocks: Application in Formation Damage-Water Blockage. *Petrophysics* **2020**, *61*, 473–481. [CrossRef]

117. Wigand, M.; Carey, J.W.; SchÜTt, H.; Spangenberg, E.; Erzinger, J. Geochemical effects of CO_2 sequestration in sandstones under simulated in situ conditions of deep saline aquifers. *Appl. Geochem.* **2008**, *23*, 2735–2745. [CrossRef]

118. Lu, J.; Kharaka, Y.K.; Thordsen, J.J.; Horita, J.; Karamalidis, A.; Griffith, C.; Hakala, J.A.; Ambats, G.; Cole, D.R.; Phelps, T.J.; et al. CO_2–rock–brine interactions in Lower Tuscaloosa Formation at Cranfield CO_2 sequestration site, Mississippi, USA. *Chem. Geol.* **2012**, *291*, 269–277. [CrossRef]

119. Shi, Z.; Sun, L.; Haljasmaa, I.; Harbert, W.; Sanguinito, S.; Tkach, M.; Goodman, A.; Tsotsis, T.T.; Jessen, K. Impact of Brine/CO_2 exposure on the transport and mechanical properties of the Mt Simon sandstone. *J. Pet. Sci. Eng.* **2019**, *177*, 295–305. [CrossRef]

120. Kim, K.; Makhnenko, R.Y. Short- and Long-Term Responses of Reservoir Rock Induced by CO_2 Injection. *Rock. Mech. Rock. Eng.* **2022**, *55*, 6605–6625. [CrossRef]